Evaluation of a wind tunnel designed to investigate the response of evaporation to changes in the incoming longwave radiation at a water surface. I. Thermodynamic characteristics

5   Michael L. Roderick[1], Chathuranga Jayarathne[1], Angus J. Rummery[1], Callum J. Shakespeare[1,2]

[1]Research School of Earth Sciences, Australian National University, Canberra, Australia, 2601.
[2]ARC Centre of Excellence for Climate Extremes, Australian National University, Canberra, Australia, 2601.

Correspondence to: Callum J. Shakespeare (callum.shakespeare@anu.edu.au)

Abstract. To investigate the sensitivity of evaporation to changing longwave radiation we developed a new experimental
10   facility that locates a shallow water bath at the base of an insulated wind tunnel with evaporation measured using an accurate
digital balance. The new facility has the unique ability to impose variations in the incoming longwave radiation at the water
surface whilst holding the air temperature, humidity and wind speed in the wind tunnel at fixed values. The underlying
scientific aim is to isolate the effect of a change in the incoming longwave radiation on both evaporation and surface
temperature. In this initial paper we describe the configuration and operation of the system and outline the experimental design
15   and approach. We then evaluate the thermodynamic properties of the new system and demonstrate that the evaporation, air
temperature, humidity and wind speed are measured with sufficient precision to support the scientific aims. We find that the
shallow water bath naturally adopts a steady state temperature that closely approximates the thermodynamic wet bulb
temperature.

1 Introduction

20   The Earth's climate system is in some sense like a giant heat engine with water evaporating at the relatively warm surface and
condensing at a relatively colder altitude in the atmosphere. With water the dominant surface cover on the planet, the water
cycle emerges as a central component of both the thermodynamics and dynamics of the climate system (Peixoto and Oort,
1992; Pierrehumbert, 2010). Traditionally, the evaporation of water at the surface has been described using bulk-formulae with
the evaporation held to depend on the difference in specific humidity between the (saturated) surface and (sub-saturated)
25   atmosphere, the wind speed and a transfer coefficient (WMO, 1977; Monteith and Unsworth, 2008). The use of bulk-formulae
requires measurement of the surface temperature to specify the specific humidity at the (near-saturated) surface. On that
approach, it is straight-forward, in principle at least, to conduct experiments using a controlled wind tunnel to measure the
evaporation from a water body as a function of surface temperature, specific humidity in the adjacent air and the wind speed.
It is also possible to use comprehensive field measurements to derive bulk-formulae for evaporation (e.g., Penman, 1948;

30 Thom et al., 1981; Lim et al., 2012). The same approach can be used to derive bulk-formulae for sensible heat transfer with the gradient given by the difference in temperature between the water surface and overlying air (WMO, 1977).
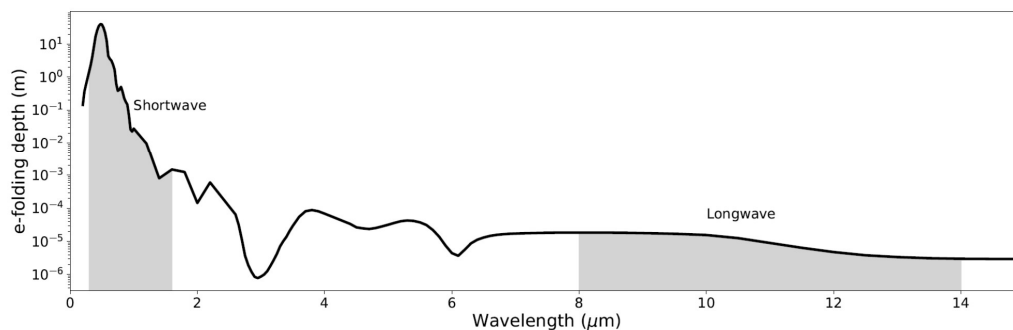
Figure 1: Characteristic penetration depth of radiation into liquid water at different wavelengths (Irvine and Pollack, 1968; Hale
35 **and Querry, 1973). Shaded regions highlight the shortwave (here taken as 0.3-1.6 µm) and longwave (here taken as 8-14 µm) regions of the electromagnetic spectrum. Note the log-scale (y-axis).**

The bulk-formulae approach, sometimes also called the mass transfer approach, does not explicitly consider the radiative fluxes. Indeed it has long been standard practice to ignore the radiative fluxes when the bulk-formula are derived (e.g., see
40 Chapter 6 in Incropera et al, 2017). However, one can construct a comprehensive energy budget for a water surface by combining the above-noted latent (i.e., proportional to evaporation) and sensible heat fluxes with the incoming and outgoing shortwave and longwave radiative fluxes and by also including energy storage in the water body. Importantly, clear liquid water is relatively transparent to shortwave radiation with a characteristic e-folding absorption depth (i.e., depth at which $1/e$ ($\sim 37\%$) of the incident radiation remains) of order 40 m at a wavelength of 0.5 µm (Fig. 1). In contrast, longwave radiation
45 has a characteristic e-folding absorption depth of only 16×10^{-6} m at a wavelength of 10 µm that is *6 orders of magnitude* smaller than for shortwave radiation (Fig. 1). It follows that most of the emitted longwave radiation must also emanate from the same 10-20 µm depth. With liquid (and solid) water having an emissivity (and hence longwave absorption) close to unity, we anticipate that longwave radiation must impact the near-surface (i.e., within 10-20 µm) energy balance on almost instantaneous time scales. To give a numerical example, assume the global annual average incoming longwave radiation at the
50 surface of ~ 342 W m^{-2} (Wild et al., 2013) were to be completely absorbed in the top 20 µm of the ocean. Without any other heat transfer, this thin layer of water would warm by around 4°C every second. Of course this warming rate is not observed which by itself implies a very efficient means of shedding that heat (by evaporation, sensible heat and outgoing longwave radiation) into the atmosphere (Monteith and Unsworth, 2008) and/or by conductive/convective fluxes into the interior of the ocean (Saunders, 1967; McAlister and McLeish, 1969). In summary there are numerous complex exchanges of heat and mass

55   happening within 10-20 μm of the ocean surface (Saunders, 1967; McAlister and McLeish, 1969; Woolf et al., 2016; Wong and Minnett, 2018). We speculate that any imbalance between the incoming and outgoing longwave radiation is likely to immediately influence the evaporative flux because those exchanges are confined to very small distances from the surface.

As noted previously, mass transfer formulations for evaporation are usually derived experimentally using measurements of

60   surface and air temperature, air humidity and wind speed but traditionally they have not directly consider the longwave radiative fluxes. We expect that a bulk formulae for evaporation from a water body could ignore the incoming and outgoing longwave radiative fluxes when they were equal because they would cancel. However, under the more common conditions, the incoming and outgoing longwave radiative fluxes would not cancel and would be potentially important for evaporation because those longwave fluxes would lead to a near-immediate response since they occur only a small (10-20 μm) distance

65   from the surface. Indeed, previous theoretical and laboratory-based research has confirmed that any difference between incoming and outgoing longwave radiative fluxes must be considered an important part of the evaporative bulk formulae (Nunez and Sparrow, 1988; Sparrow and Nunez, 1988). The implication here is that the formulation of existing bulk-formulae for evaporation (and by inference also for sensible heat) may need to be re-considered to directly include the potentially important influence of longwave radiation on evaporation. Besides the above-noted Nunez-Sparrow study, we are not aware

70   of any other experimental work on this topic.

To support an investigation of bulk-formulae we sought to develop a new experimental system that could measure and/or control the traditional variables considered in mass transfer studies of evaporation (surface temperature, humidity and temperature of the adjacent air, wind speed). The unique feature is an augmented capability to independently vary the incoming

75   longwave radiation at the water surface whilst holding the other variables fixed. The scientific rationale of this approach was to isolate the effect of a change in the incoming longwave radiation on both evaporation and surface temperature. The overall project proved to be complex because it involved both radiative and thermodynamic phenomena. In this first paper we describe the experimental wind tunnel and present our evaluation of the overall thermodynamic behaviour of the system. A forthcoming companion paper will describe and evaluate the radiative aspects of the experimental wind tunnel. The current paper is set out

80   as follows. In section 2 we describe both the design and operation of the experimental wind tunnel. In section 3 we describe the thermodynamic behaviour of the experimental wind tunnel and in section 4 we show that the shallow water bath at the centre of the wind tunnel naturally adopts a steady state temperature that closely approximates the theoretical thermodynamic wet bulb temperature. In section 5 we discuss the results and make an overall assessment of the thermodynamic performance of the new wind tunnel facility.

2 Design and Operation

In this section we describe the configuration (section 2.1) and operation of the wind tunnel (section 2.2) and conclude with a description of the experimental design (section 2.3).

2.1 Configuration of the wind tunnel
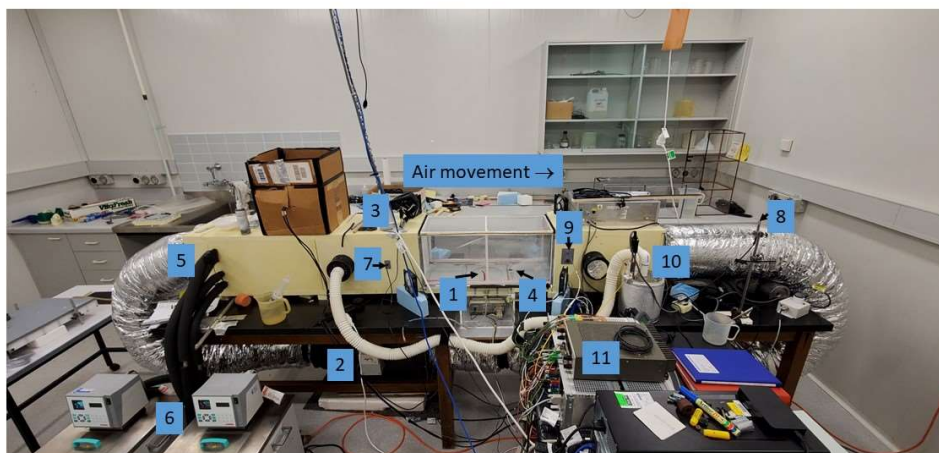
Figure 2: Photograph of the wind tunnel in the temperature controlled room of the Geophysical Fluid Dynamics Laboratory. Key numbers as follows: [1] Water bath and digital balance (AND Corporation: Model GX-6100); [2] Variable speed fan; [3] Thermal camera (FLIR: Model E50); [4] Camera Spot (used for thermal camera calibration); [5] Radiator (for air temperature control); [6] Constant temperature water bath (Julabo: Model PP50); [7] Humidity/Temperature sensor (for measuring tunnel air, VAISALA: Model HMP140); [8] Humidity/Temperature sensor (for measuring laboratory air, VAISALA: Model HMP140); [9] Temperature sensor (thermistor for measuring tunnel air, Thermometrics NTC: Model FP07DA103N); [10] Vapour source (humidifier for humidity control of tunnel air); [11] Digital controller.

After several initial attempts with various configurations the final wind tunnel layout is shown in Fig. 2 with a simplified schematic in Fig. 3. The wind tunnel was constructed of closed cell foam (density of 60 kg m⁻³, cross section of 300×300 mm, 2550 mm total length) located on a laboratory bench with a recirculating flow of air passed through heating duct located under the bench. During experiments the wind speed was set using a variable speed fan located in series along the heating duct (see [2] in Fig. 2) and measured using a hot wire anemometer (Sierra Instruments: Model No. 600, not visible in Fig. 2; U in Fig. 3). The same closed cell foam material was used to construct a shallow water bath (diameter 200 mm, 8 mm depth, see

[1] in Fig. 2) that sat on a digital balance. The shallow water bath and the base of the tunnel elsewhere were painted using

105 commercial waterproof paint (longwave emissivity ~ 1, results not shown) to ensure the surface was impermeable to water. The rate of change of the mass of water was used to measure the evaporation rate from the shallow water bath (E in Fig. 3). To calibrate the incoming longwave radiation at the water surface, the shallow water bath could be removed and replaced by a radiometer (Kipp and Zonen: Model CNR1 net radiometer) that was custom mounted onto a closed cell foam base so that the centre of the longwave sensor was at the same horizontal and vertical position as the centre of the water surface in the

110 shallow water bath. During routine evaporation experiments, the radiometer was located in the laboratory (but outside the tunnel) and used to measure the incoming longwave radiation at the top of the outer film ($R_{i,F2}$ in Fig. 3).
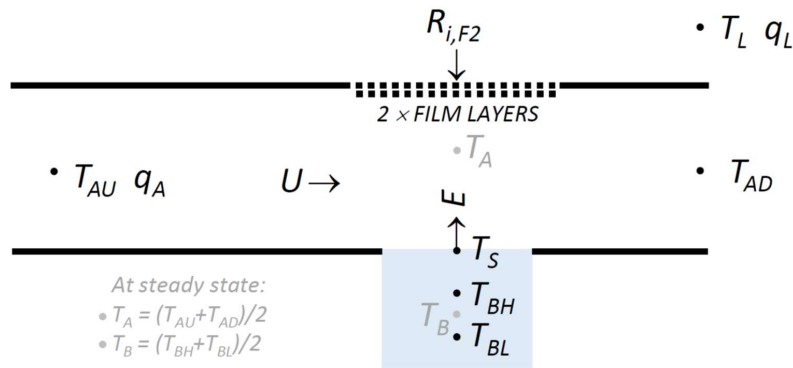
Figure 3: Schematic drawing showing the measured properties (•) and fluxes (→) in the wind tunnel facility. See main text for details.

115

Two thermocouples (Thermocouples Direct: Model KM1(118)0.25x250) were inserted into the shallow water bath to measure the bulk (liquid) water temperature. The 'high' sensor was located 5 mm from the bottom (T_{BH} in Fig. 3) and the 'low' sensor was located 1 mm from the bottom (T_{BL} in Fig. 3) of the shallow water bath. The design intent was for the base of the shallow water bath to form a 'no heat flux' condition (i.e., an adiabatic lower boundary). By measuring the temperature in the closed

120 cell foam below the shallow water bath using a temperature probe during typical experiments (results not shown) we concluded that the design intent was achieved because of the excellent insulation properties of the closed cell foam. Directly above the shallow water bath we located a removable PVC frame (730 mm length) covered by two layers of polyethylene (i.e., plastic) film (Fig. 2) enclosing a 10 mm air gap between them, with each film being 0.022 mm thick. The use of two layers of film allowed us to avoid condensation of water onto the film (see discussion in section 2.3). We placed silica gel desiccant beads

125   in the air gap to further avoid condensation. Above the PVC frame (and outside the film) we located a thermal camera (see [3] in Fig. 2) to measure the surface (skin) temperature of water during evaporation experiments (T_S in Fig. 3). On the downstream side of the shallow water bath we installed a small circular copper plate (the 'spot', see [4] in Fig. 2) painted with commercial paint (longwave emissivity ~ 1, results not shown) to assist with calibration of the thermal camera (FLIR: Model E50, see [3] in Fig. 2). The copper 'spot' (~ 1 mm thick) was clearly visible in the thermal imagery and we drilled a hole and inserted a

130   thermocouple (Thermocouples Direct: Model KM1(118)1.0x250) into the underside of the copper 'spot' to assist with calibration of the thermal camera measurements. As described below, the temperature, humidity and wind speed of air within the tunnel could all be held fixed at user-defined levels. By locating the entire wind tunnel facility within a temperature controlled room (length 6700 mm, width 4600 mm, height 3000 mm) within the Geophysical Fluid Dynamics Laboratory we were able to vary the incoming longwave radiation arriving at the top of the plastic film ($R_{i,F2}$ in Fig. 3) by changing the air

135   temperature (T_L in Fig. 3) – and thus the temperature of all surfaces – in the room. By this design we were able to change the incoming longwave radiation arriving at the top of the film independently of the air temperature, humidity and wind speed within the tunnel. Note that the incoming longwave radiation at the top of the film ($R_{i,F2}$ in Fig. 3) is effectively the blackbody radiation emitted by the walls of the temperature controlled room.

140   In more detail, the air temperature in the tunnel was controlled using a commercial radiator installed within the tunnel (see [5] in Fig. 2) and connected via a recirculating flow to an external constant temperature water bath (see [6] in Fig. 2). As the air stream moved through the constant temperature radiator, heat conduction ensured the air temperature in the tunnel rapidly equilibrated with the radiator temperature. We measured the temperature and humidity of the air stream after it had passed through the radiator (see [7] in Fig. 2; T_{AU} and q_A in Fig. 3). Following that the air was passed through a block of plastic straws

145   of cross section of 300×300 mm and length of 150 mm with each individual straw in the block having a diameter of 4 mm. This block, commonly known as a 'laminarizer' (e.g., Huang et al., 2017) engineered a near-laminar flow of air (verified using smoke experiments, results not shown) over the shallow water bath. The air temperature was measured downstream of the shallow water bath (see [9] in Fig. 2; T_{AD} in Fig. 3). Finally, we measured the temperature and specific humidity of air in the laboratory (external to the tunnel) (see [8] in Fig. 2; T_L and q_L in Fig. 3). The humidity sensors (see [7] and [8] in Fig. 2; and

150   respectively q_A and q_L in Fig. 3) measured the relative humidity and this was converted to specific humidity by assuming the moist air to be an ideal gas with the total air pressure set to 1 bar (i.e., the climatological average for Canberra, Australia). Although not discussed in detail here (see the forthcoming radiative paper), for completeness we also note the measurement of the 'skin' temperature of water at the surface of the shallow water bath (T_S in Fig. 3) using the thermal camera (see [3] in Fig. 2).

155

All sensors were connected to a digital sampling system (see [11] in Fig. 2) that was interfaced to a standard digital computer with all data sampling and acquisition controlled using the LabVIEW (National Instruments Corporation) software package. The one exception was the thermal camera which was operated independently using instrument-specific software available

(by purchase) from the manufacturer. In post-processing, the thermal camera measurements of surface temperature were
160   merged into the experimental database using time stamps embedded within both data streams.

2.2 Operation of the wind tunnel

During experiments both the air temperature and wind speed in the tunnel proved relatively easy to control. The most
challenging variable to control was the humidity of air within the tunnel. The experiments were designed so that the pre-
determined specific humidity of the tunnel air generally exceeded that in the laboratory which required the addition of water
165   vapour to the tunnel air to arrive at the pre-determined humidity. For that purpose, we used an independently controlled
electrical heater element immersed in a water bath to generate warm water vapour that could be vented into the tunnel on
demand (see [10] in Fig. 2). Occasionally we would overshoot the pre-determined specific humidity of the tunnel air and we
used a condenser to remove excess water vapour. For that we installed a temperature-controlled copper plate on the base of
the tunnel (not visible but located downstream of [10] in Fig. 2). The copper plate was connected to another constant
170   temperature water bath (again not visible but of the same type as [6] in Fig. 2) that recirculated water through a network of
channels within the copper plate. By cooling the copper plate as required we were able to engineer a cold surface onto which
excess water vapour could be condensed and routed to an external drain on demand.

Typical operations would begin each day by filling the shallow water bath to a pre-determined mass (we used ~ 250 (± 25) g
175   of water and equivalent to ~ 8 mm water depth) and by allowing the externally controlled radiator (see [5] and [6] in Fig. 2) to
come to a steady state temperature. Each of the numerous temperature sensors were then checked against the portable
laboratory reference (HART Scientific: Model 1521) and any necessary (minor) offset adjustments made within the LabVIEW
control software. During the experiments all data elements were sampled at 30 Hz and then averaged to successive 10 second
time steps within the LabVIEW control software. The same sampling protocol was used for the thermal imagery.

2.3 Experimental design

As part of the overall experimental program, we conducted evaporation sub-experiments at ten pre-determined combinations
of air temperature and specific humidity (Fig. 4). The original aim was to sample a regular grid of temperature (15, 25, 35, 45
°C) and specific humidity (5, 15, 25, 35 g kg^{-1}) co-ordinates in the sub-saturated part of the phase diagram. The lower bound
for the specific humidity was increased from 5 to 7 g kg^{-1} to avoid (where possible) circumstances where moisture had to be
185   extracted from air in the tunnel. To ensure reliable surface temperature measurements using the thermal camera we avoided
experiments where condensate formed on the film. The main problem with condensate is that liquid water droplets absorb
most of the incoming longwave radiation (e.g., Fig. 1) but re-emit longwave radiation at the local water droplet temperature
which interfered with the thermal camera measurements. We were unable to complete the 35°C and 25 g kg^{-1} sub-experiment
due to condensation occasionally forming on the interior film at the highest wind speed. Instead we completed that sub-

190   experiment at 35°C and 20 g kg⁻¹ (Fig. 4). The same situation also occurred for the highest humidity attempted at 45°C and

we completed that sub-experiment at a combination of 45°C and 30 g kg⁻¹ (Fig. 4). The experiment at 45°C and 7 g kg⁻¹ was

completed but unfortunately failed a subsequent quality control check.
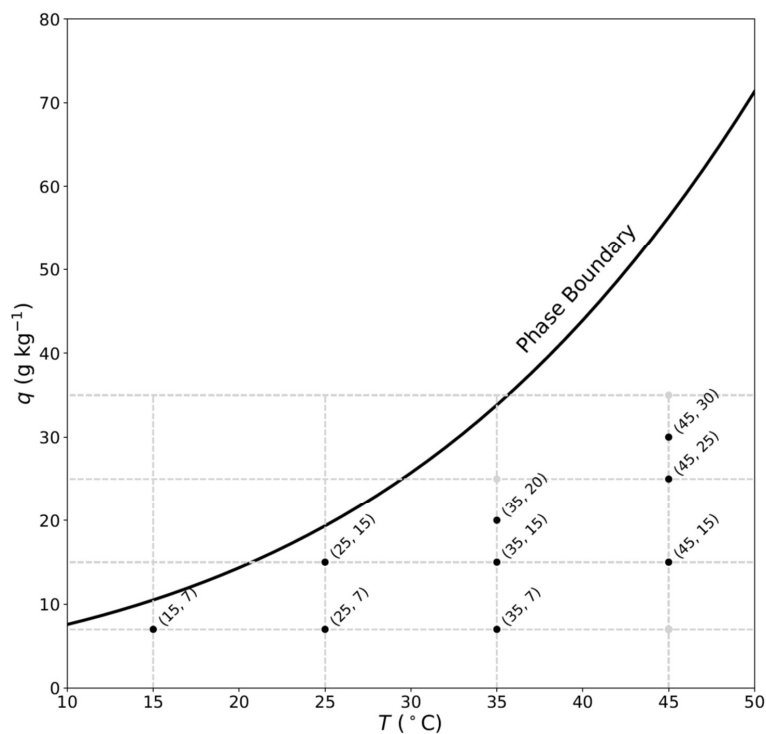
Figure 4: The nine combinations of air temperature and specific humidity (●) used in the final evaporation experiments.
195   **The full line denotes the liquid-vapour phase boundary (i.e., saturation curve, total pressure of 1 bar) computed using an empirical equation (Huang, 2018). The three grey dots (◌) highlight experiments that were attempted but not satisfactorily completed.**

At each of the nine air temperature-specific humidity combinations (Fig. 4) we varied the wind speed over five discrete steps

200   (0.5, 1.0, 2.0, 3.0, 4.0 m s⁻¹). To control the incoming longwave radiation at the top of the film ($R_{i,F2}$ in Fig. 3) we set the

laboratory air temperature on the room controller to be either 19°C which we denoted the 'Ambient' condition or to 31°C

which we denoted the 'Forced' condition. A change between the 'Ambient' and 'Forced' condition took several hours to

equilibrate within the temperature-controlled room and was usually completed overnight. The typical procedure for a given

incoming longwave forcing and air temperature-specific humidity combination in the tunnel was to begin at a wind speed of
205   0.5 m s^{-1} (or sometimes 4 m s^{-1}) and then wait for the steady state condition (typically an hour or so, see the following section)
before changing to the next wind speed and so on. Typically (but not always), we could complete the experiments for the five
pre-determined wind speeds at a given temperature-specific humidity combination within a single day. In total, the
experimental program generated 90 individual 'steady state' results (i.e., 9 air temperature-specific humidity combinations ×
5 wind speeds × 2 incoming longwave conditions). Experiments are named using the nomenclature *Forcing-T-q-U*. For
210   example Ambient-T15-q7-U2 is an experiment done using the Ambient forcing (i.e., laboratory air temperature ~ 19°C) with
target tunnel conditions at 15°C and 7 g kg^{-1} with wind speed of 2 m s^{-1}. The nomenclature Forced-T15-q7-U2 refers to the
same conditions but with laboratory air temperature set to 31°C.

3 Thermodynamic Evaluation

In this section we describe the approach to steady state (section 3.1) and characterise the variability in key measured variables
215   once at steady state (section 3.2). We conclude the section with a brief overview of the response of latent heat flux (i.e., the
evaporative flux) and bulk water temperature to wind speed that is required to understand the overall context of the experiments
(section 3.3).

3.1 The approach to steady state

We conducted two (related) experiments to demonstrate the approach to steady state under the same conditions (tunnel air
220   temperature of 35°C, specific humidity of 25 g kg^{-1} and wind speed of 2 m s^{-1}). Figure 5 depicts the first experiment. The mean
air temperature in the laboratory was ~ 19°C (i.e., the 'Ambient' condition) and varied with an amplitude of ~ 1°C over a
period that was ~ 900 s (i.e., 15 mins) in this example (Fig. 5a). This periodic variation was a consequence of the cooling
control system deployed in the temperature controlled laboratory whose settings could not be altered. The period also varied
with the external weather conditions. Despite that periodicity, the air temperature in the tunnel was controlled within a much
225   tighter range and was held close to the target temperature of 35°C (T_{AU}, T_{AD} in Fig. 5a). Similarly, the specific humidity of air
in the laboratory also showed the same periodic behaviour (period ~ 900 s, see q_L in Fig. 5c), but again, the specific humidity
of air in the tunnel was controlled within a much tighter range (q_A, Fig. 5c). The incoming longwave radiation at the top of the
tunnel was measured using the radiometer ($R_{i,F2}$, Fig. 5e) and also varied over the same 900 s period. The direct measurement
of $R_{i,F2}$ was very close to the theoretical black body radiation at the temperature of the laboratory air as expected (see blue line
230   in Fig. 5e).
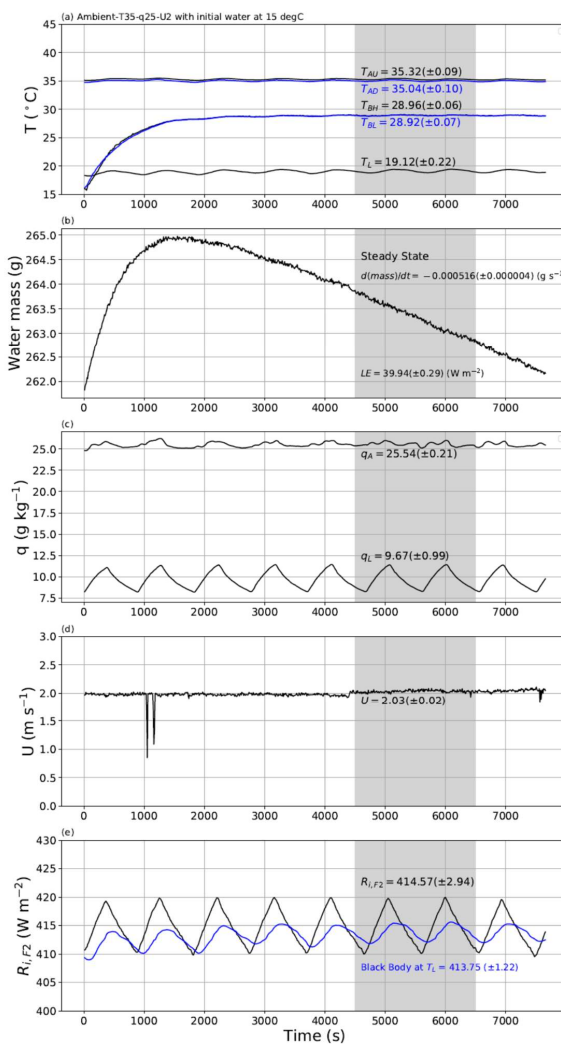
Figure 5: An experimental demonstration of the approach to steady state. The experiment began with water at 15°C in the shallow water bath (T_{BH}, T_{BL} in (a)) with target conditions for air in the tunnel set to Ambient-T35-q25-U2. The plots document the approach to steady state (4500-6500 s) for the evolution of (a) temperature of air in the tunnel (T_{AU} (black), T_{AD} (blue)), temperature of water in the shallow water bath (T_{BH} (black), T_{BL} (blue)) and temperature of air in the laboratory (T_L), (b) mass of water in shallow water bath with calculated rate of change (via linear regression) and the associated latent heat flux (LE), (c) specific humidity of air in the tunnel (q_A) and in the laboratory (q_L), (d) wind speed (U) and (e) the measured incoming longwave radiation at the top of tunnel ($R_{i,F2}$) compared with theoretical black body radiation at laboratory air temperature (T_L, blue). The numbers on each panel indicate the steady state averages (± 1sd).

235
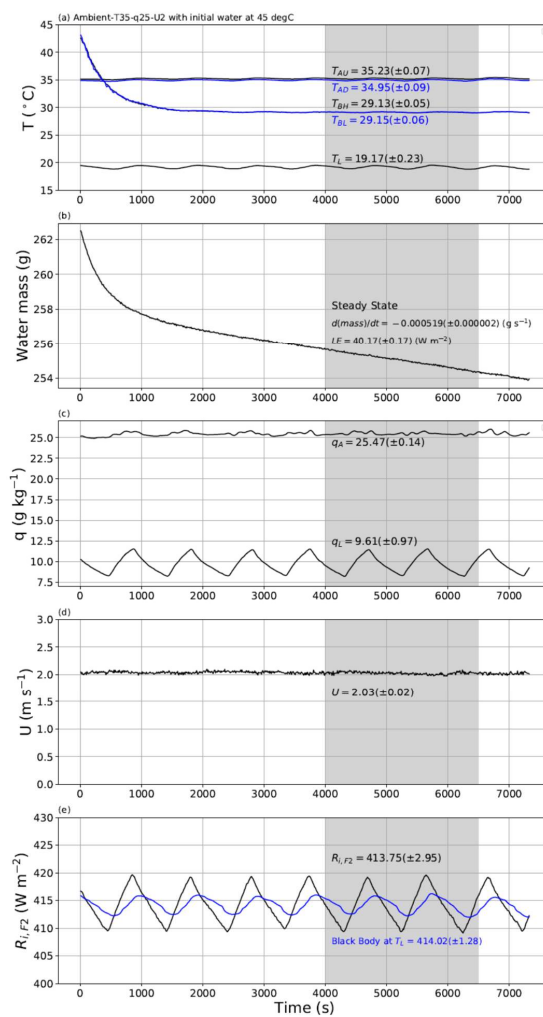
240

Figure 6: Same as Figure 5 but starting with water at 45°C in the shallow water bath.

Of most interest here is the approach to steady state in terms of the evaporation (Fig. 5b) and the water temperature in the shallow water bath (Fig. 5a). Note that this first experiment was initialised with ~ 15°C water in the shallow water bath (Fig. 5a, T_{BH}, T_{BL}). Inspection of Fig. 5a shows that the temperature of water in the shallow water bath increased at an exponentially

245

decreasing rate towards a steady state some 4500 s from the beginning. Concurrently, with the initial conditions having colder water in the shallow water bath (15°C) than in the tunnel air (35°C), the initial evaporation rate was negative (i.e., condensation occurred) for the first 1500 s with a steady state evaporation rate being reached around 3000 s after the beginning of the experiment. We repeatedly observed that the time taken to reach a steady state for evaporation was somewhat shorter than the
250   time taken for the temperature of bulk water in the shallow water bath to reach steady state. Once at steady state, we calculated averages for all variables using the same user-specified time interval. Recall that the instruments were all sampled at 30 Hz and then averaged to successive 10 s periods. Hence for this example experiment, the steady state average was calculated using 201 samples (i.e., (6500-4500)/10 + 1) and the standard deviation was also calculated using those same 201 samples.

255   Once at steady state, the bulk water in the shallow water bath had a near-uniform temperature as anticipated (T_{BH} and T_{BL} in Fig. 5a). Accordingly, we characterised the steady state water bath temperature (T_B in Fig. 3) as the average over the two depths. In this particular experiment we note that the steady state air temperature in the tunnel was slightly warmer in the upstream location (T_{AU}) relative to the downstream location (T_{AD}) (Fig. 5a). This was expected since the upstream air was closer to the radiator with the air then passing through the non-insulated part of the tunnel (i.e., the part covered with plastic
260   film above the shallow water bath, see Fig. 3) before entering the insulated tunnel again where the downstream air temperature was measured (T_{AD} in Fig. 4). We consistently found that the upstream tunnel air (T_{AU}) was slightly warmer (colder) than the downstream tunnel air (T_{AD}) when the air in the tunnel was warmer (colder) than air in the laboratory (T_L) (results not shown). In other words, the part of the wind tunnel directly below the film was not quite adiabatic (because of the design). With that understanding we characterised the steady state tunnel air temperature immediately above the shallow water bath (T_A in Fig.
265   3) as the average of the measured upstream and downstream values.

We repeated the first experiment but this time we placed water at an initial temperature of ~ 45°C in the shallow water bath (Fig. 6). This second experiment shows that the initial evaporation rate was greater than the final steady state evaporation rate (Fig. 6b) while the water in the shallow bath progressively cooled to a final steady state temperature reached some 4000 s after
270   the beginning of the experiment (Fig. 6a). Again, the temperature of bulk water in the shallow water bath was uniform at steady state to within measurement uncertainty (T_{BH} and T_{BL} in Fig. 6a). Importantly, the final steady state water bath temperature was more or less the same (Fig. 6a; $T_B = 29.14$ (±0.06) °C) as in the earlier experiment (Fig. 5a; $T_B = 28.94$ (±0.07) °C) despite the initial temperature of water in the shallow water bath being very different. Similarly, the steady state latent heat flux was also the same (Fig. 6b; $LE = 40.17$ (±0.17) W m^{-2}) as in the earlier experiment (Fig. 5b; 39.94 (±0.29) W m^{-2}). We show later
275   (section 4) that the water bath has a preferred steady state temperature that is more or less equivalent to the thermodynamic wet bulb temperature.

3.2 Variability during steady state conditions
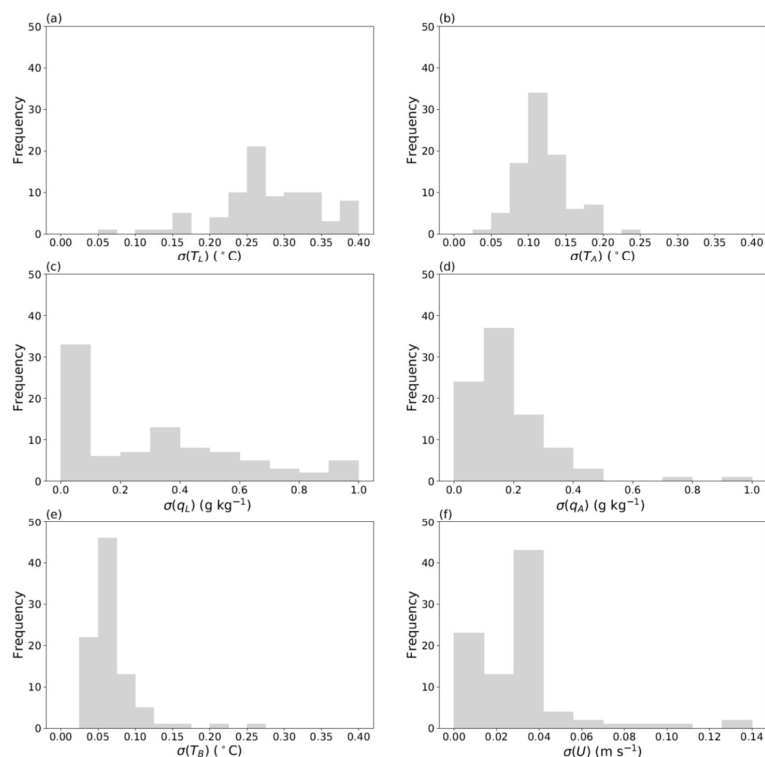
Figure 7: Steady state variability of six key variables. Histograms show the steady state standard deviation over all 90 experiments (i.e., 9 air temperature-specific humidity combinations × 5 wind speeds × 2 incoming longwave conditions) for air temperature in the (a) laboratory (T_L) and the (b) wind tunnel (T_A), specific humidity of air in the (c) laboratory (q_L) and the (d) wind tunnel (q_A), (e) average bulk water temperature in the shallow water bath (T_B) and the (f) wind speed (U).

The precision of the measurements depends on the intrinsic characteristics of the instruments and temporal variability during the designated steady state period. Over all 90 experiments, the length of the steady state period varied from 850 to 3300 s (~ 14 to 55 minutes). To minimise the impact of the periodic variation in T_L (Fig. 5a, 6a) we (visually) selected the steady state period to be an integer multiple of the period wherever possible (e.g., Figs 5 and 6). Overall we found temporal variability during the steady state period to be the dominant source of uncertainty in the steady state averages. To summarise that uncertainty, we show the steady state standard deviation for six key variables across all of the 90 evaporation experiments (Fig. 7). The larger range in standard deviation for the steady state temperature of laboratory air (T_L, Fig. 7a) compared to that

for the tunnel air (T_A, Fig. 7b) and the water bath (T_B, Fig. 7e) is consistent with the more tightly controlled conditions within the wind tunnel relative to the surrounding laboratory. The same held for humidity with the steady state standard deviation of the specific humidity of laboratory air (q_L, Fig. 7c) being substantially larger than for the tunnel air (q_A, Fig. 7d). For most experiments (88 out of 90) the steady state standard deviation for tunnel air specific humidity (q_A, Fig. 7d) was less than 0.5 g

295   kg^{-1}. However, for two experiments under very extreme conditions (i.e., the highest temperature, specific humidity and wind speed combination) we experienced considerable difficulty in controlling the specific humidity (Ambient-T45-q25-U4, $\sigma(q_A)$ = 0.90 g kg^{-1}; Ambient-T45-q30-U4, $\sigma(q_A)$ = 0.73 g kg^{-1}). Despite numerous attempts we were unable to decrease the steady state standard deviation for those two experiments. The wind speed remained very tightly controlled (Fig. 7f).
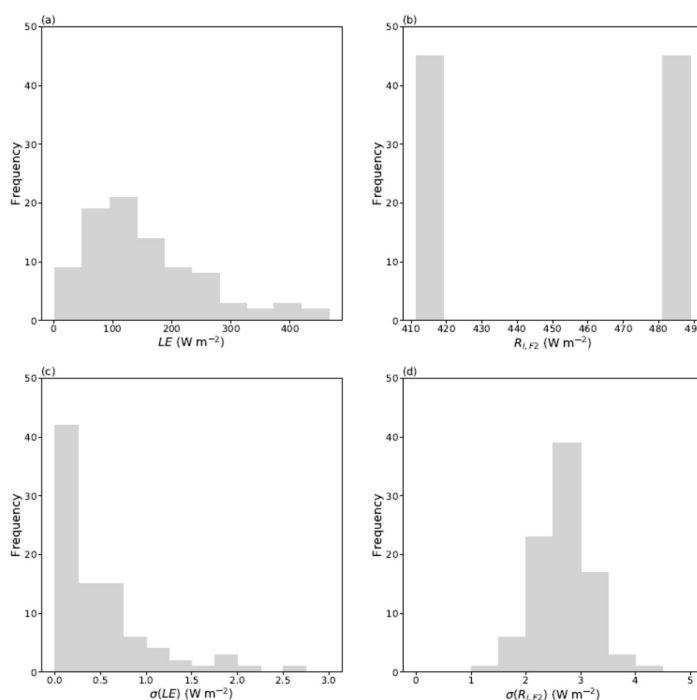
300

Figure 8: Magnitude and uncertainty for the key thermodynamic fluxes. Steady state averages for (a) latent heat flux (*LE*) and (b) incoming longwave radiation at the top of the film ($R_{i,F2}$) along with the respective steady state standard deviations (c) $\sigma(LE)$ and (d) $\sigma(R_{i,F2})$.

305   A summary for the key thermodynamic fluxes is shown in Fig. 8. Over all 90 experiments the steady state *LE* varied from 2.1 to 465.6 W m-2 (Fig. 8a) while the standard deviation for LE was less than 2.6 W m^{-2} and for three-quarters of the data it was

less than 1 W m^{-2} (Fig. 8c). The incoming longwave radiation at the top of the film was either ~ 415 W m^{-2} (blackbody at the ambient T_L of 19°C) or ~ 485 W m^{-2} (blackbody at the forced T_L of 31°C) (Fig. 8b) while the overall steady state standard deviation ranged from 1.2 to 4.2 W m^{-2} (Fig. 8d).

310

A very general overview of variability during the steady state period can be obtained by calculating the rate of heat storage (i.e., enthalpy flux) in the shallow water bath. We calculate the change in enthalpy of the water mass in the bath over the steady state time period using the difference between the averages of the last ten temperature measurements and the first ten measurements. Dividing that enthalpy difference by the steady state time period and by the surface area of the water surface

315 we have the equivalent rate of heat storage in the shallow water bath denoted G (with units of W m^{-2}). Note that a perfect steady state condition would have G equal to zero. Over all 90 experiments, G ranges from -5.0 to +3.4 W m^{-2} with an overall mean of zero (Fig. 9).
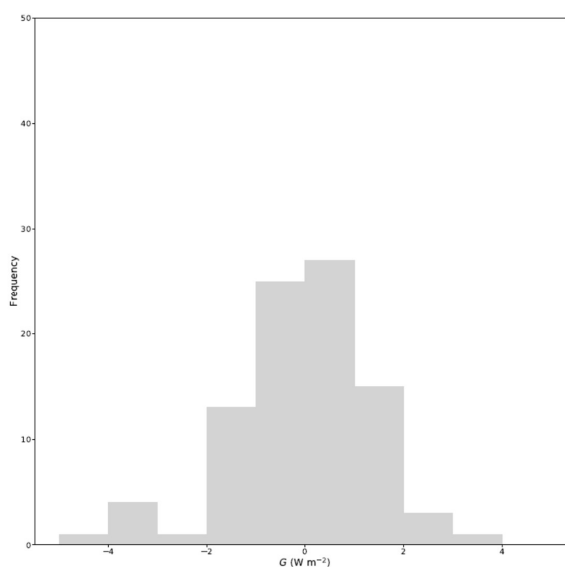
320   **Figure 9: Histogram of the rate of enthalpy storage in the shallow water bath over the steady state period (G).**

3.3 Response of latent heat flux and bulk water temperature to wind speed
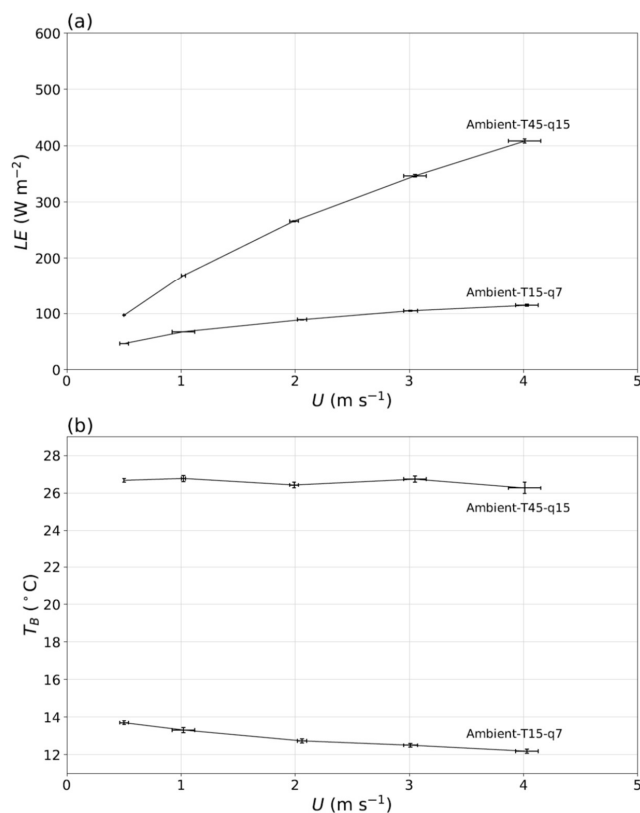
325

**Figure 10: Response of the steady state (a) latent heat flux (*LE*) and (b) water temperature in the shallow water bath (*T*$_B$)
to wind speed (*U*) in two typical evaporation experiments. The error bars denote ±2sd (i.e., 95% confidence interval).**

One key aspect of the experiment was to document how the (steady state) evaporation rate and bulk water temperature in the

330   shallow water bath responded to wind speed. To gain an initial overview we use data from two laboratory experiments (Fig.
10). Briefly, the latent heat flux (and hence evaporation rate) increased substantially with wind speed (Fig. 10a) in all
experiments. However, to zeroth order, the steady state bulk water temperature did not respond appreciably to variations to
wind speed and hence did not respond strongly to changes in evaporation (Fig. 10b). In more detail, for some experiments
(depending on the temperature-specific humidity combination) we found T_B to be relatively insensitive to U (Fig. 10b,

335   Ambient-T45-q15) while for other experiments we found a slight cooling of T_B with U (Fig. 10b, Ambient-T15-q7). Other
experiments (shown later in Fig. 12) showed a slight warming of T_B with U. The main point being that the latent heat flux

increased markedly with U (as expected) but the bulk temperature in the shallow water bath was more or less independent of U. This finding will be discussed in more detail in the following section.

4 Comparison with the thermodynamic wet bulb temperature

340   In this section we describe the calculation of wet bulb temperature (section 4.1) followed by a comparison of the temperature of the shallow water bath with the thermodynamic wet bulb temperature (section 4.2).

4.1 Calculating the thermodynamic wet bulb temperature

The concept of the wet bulb temperature assumes a closed adiabatic system containing moist air and a source of liquid water. In the adiabatic enclosure, the heat required to change the moisture content of the air (i.e., latent heat) is taken as sensible heat

345   from the moist air but the sum of the latent and sensible heat remains constant (Monteith and Unsworth, 2008). Hence any increase (decrease) in moisture content results in a decrease (increase) in air temperature but the overall enthalpy remains constant. The theoretical wet bulb temperature (T_W) is the temperature when the moist air becomes saturated under the adiabatic constraint. Using e (Pa) as the symbol for vapour pressure, the usual relation between the measured dry bulb air temperature (T_A) and vapour pressure (e_A) and the theoretical wet bulb temperature (T_W) is given by (Monteith and Unsworth, 2008),

350    $$e_W = e_A + \gamma(T_A - T_W) \quad , \tag{1}$$

with e_W (Pa) the saturation vapour pressure at T_W (i.e., $e_W = e_{sat}(T_W)$) and the (so-called) psychrometer constant γ (Pa K^{-1}) given by,

$$\gamma = \frac{P\,c_P}{\varepsilon\,L} \quad . \tag{2}$$

with P the total air pressure, c_P the specific heat of air, ε the ratio of the molecular mass of water to air (~ 0.622) and L the

355   latent heat of vaporisation. In many practical applications the specific heat is often taken as that for dry air but the theory requires the integrals to be taken over the actual (moist) air (Monteith and Unsworth, 2008; Greenspan and Wexler, 1968). With the specific heat for moist air slightly larger than for dry air and L declining slightly with temperature, the numerical value for γ at a total pressure of 1 bar is 66 Pa K^{-1} at 15°C. At 45°C in completely dry air γ is 68 Pa K^{-1} and increases to 71 Pa K^{-1} in saturated air (Fig. A1, Appendix A). The results presented here are not especially sensitive to this numerical value and

360   we use a constant value for γ (= 68 Pa K^{-1}) for all subsequent calculations in this paper. To compute T_W we adopt a recently developed empirical formula for the saturation vapour pressure as a function of temperature (Huang, 2018) and used a numerical iteration technique to solve Eqn (1).

4.2 Comparing the thermodynamic wet bulb with the bulk water temperature

We first calculate T_W for each of the nine temperature-humidity combinations using experiments conducted under ambient

365   conditions at a wind speed of 2 m s^{-1} (Fig. 11). It is immediately clear that the steady state bulk water temperature is very

similar to the theoretical thermodynamic wet bulb temperature in all experiments. The difference between T_B and T_W varies from -1.3°C to 1.3°C and is on average (= -0.3°C) very close to zero. Differences between T_W and T_B are expected, because as noted previously, the experimental system was not designed to be adiabatic, i.e., it has a (non-adiabatic) plastic film section that allows us to change the incoming longwave radiation independently of conditions inside the tunnel. In more detail, it is

370 also clear from Fig. 11 that for very low T_B (e.g. $T_B \sim 13°C$) we typically have $T_B > T_W$ while the opposite holds for the highest values of T_B, i.e., $T_B < T_W$.
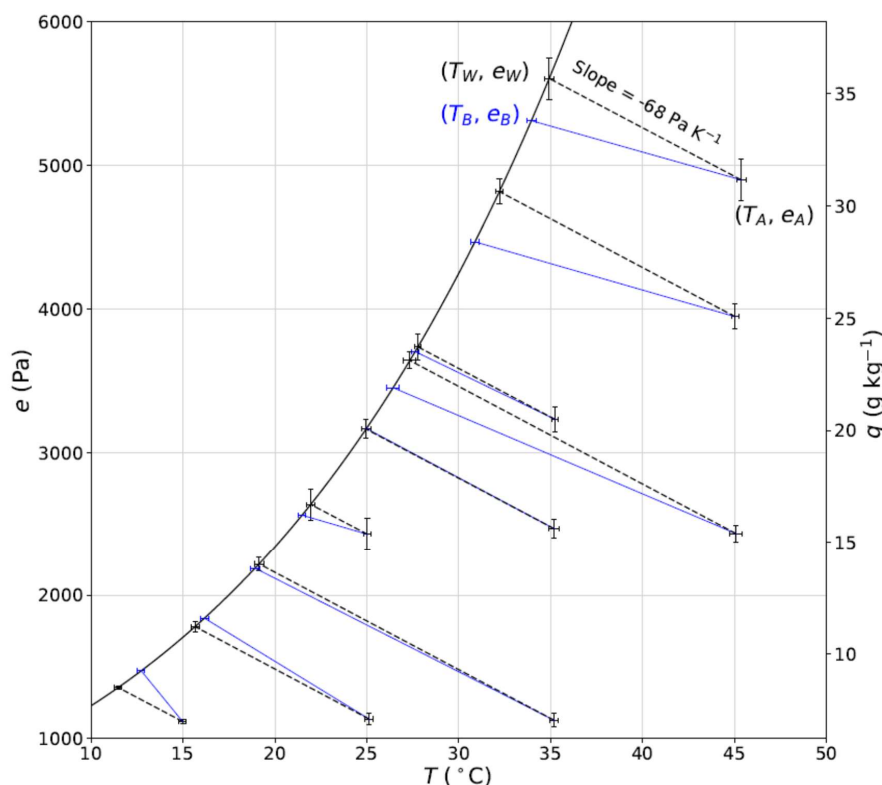
Figure 11: Comparison of observed water bath temperature (T_B) with the thermodynamic wet bulb temperature (T_W). Plot uses all
375 **experimental data at a wind speed of 2 m s^{-1} under the ambient forcing (n = 9). T_W is calculated from observations (T_A, e_A) using the assigned (adiabatic) slope (dashed line: -68 Pa K^{-1}) per Eqn (1) with e_W (= $e_{sat}(T_W)$) the saturation vapour pressure. The full blue line links the observed air properties (T_A, e_A) with the observed bulk water temperature (T_B) on the liquid-vapour saturation curve with e_B (= $e_{sat}(T_B)$) the saturation vapour pressure. The error bars denote ±2sd (i.e., 95% confidence interval). Note that we use the same error bars for (T_W, e_W) as for (T_A, e_A).**

380
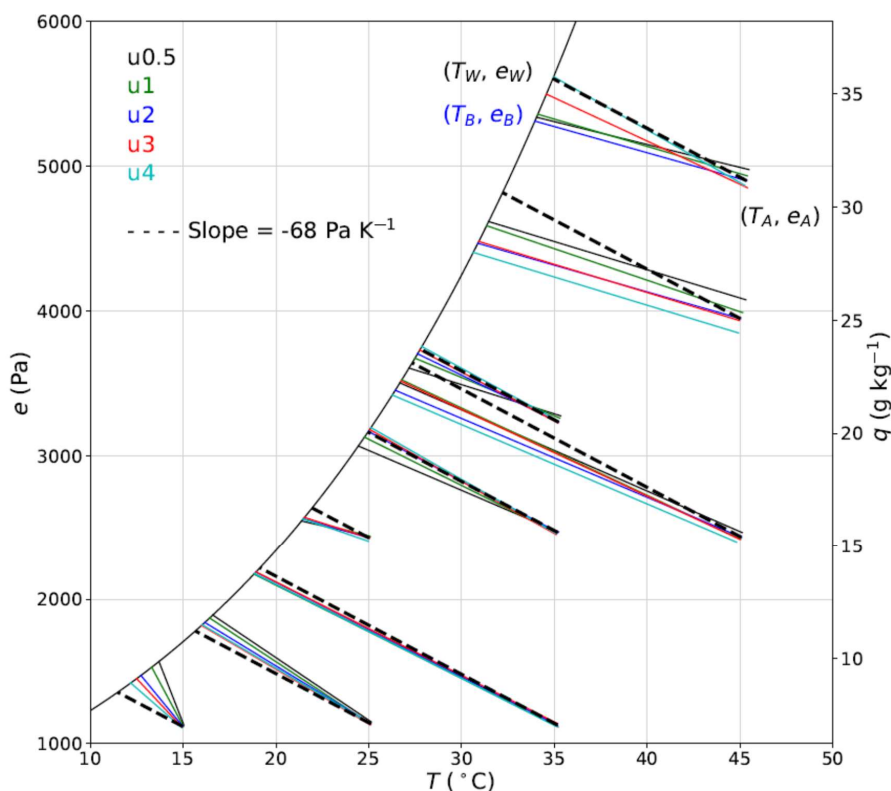
Figure 12: Comparison of observed water bath temperature (T_B) with the thermodynamic wet bulb temperature (T_W). This is the same as Fig. 11 but now using all wind speeds (U = 0.5, 1, 2, 3, 4 m s⁻¹; see legend) under the ambient forcing (n = 45). T_W is calculated from observations (T_A, e_A) at a wind speed of 2 m s⁻¹ using the assigned (adiabatic) slope (dashed line: -68 Pa K⁻¹) per Eqn (1) with e_W (= $e_{sat}(T_W)$) the saturation vapour pressure. The full lines link the observed air properties (T_A, e_A) with the observed bulk water temperature (T_B) on the liquid-vapour saturation curve with e_B (= $e_{sat}(T_B)$) the saturation vapour pressure. Error bars not shown for clarity.

385

To investigate further, in Fig. 12 we show the same data as in Fig. 11 but now using all available wind speeds. Several important

390   thermodynamic features are evident in Fig. 12. Firstly, the results confirm the previous statement that wind speed had little

impact on the bulk water temperature. The largest variation in bulk water temperature with wind speed at a given T-q

combination was ~ 2°C at T15-q7 (Fig. 12) while for most sub-experiments the impact of wind speed on bulk water temperature

was much smaller. Secondly, the spread of T_A and especially e_A data for a given sub-experiment documents the difficulty in

controlling the conditions in the tunnel. For example, for the T45-q25 experiment, the lines for different wind speeds are
395 essentially parallel but all have a slightly different specific humidity, reflecting the difficulty we had in controlling the specific
humidity in the tunnel. For that reason, when comparing the observed bulk water temperature with the calculated wet bulb
temperature it is more relevant to compare the slopes both within and between sub-experiments. When averaged over all
observations we report an average slope of -71 Pa K^{-1} that is very close to the theoretical adiabatic slope of -68 Pa K^{-1}. This
expanded plot also confirms the previously noted pattern that for very low T_B (e.g. $T_B \sim 13°C$) we typically have $T_B > T_W$ while
400 the opposite holds for the highest values of T_B, i.e., $T_B < T_W$. At intermediate values of T_B there is very close agreement between
T_B and T_W because T_B is then closer to the external laboratory temperature ($T_L \sim 19°C$ under 'Ambient' forcing) and the system
more closely approximates an adiabatic enclosure.

5 Discussion

After much experience, we were able to operate the wind tunnel and achieve the target wind speed and air temperature for a
405 given sub-experiment relatively easily. The precision of air and bulk water temperature measurements in the tunnel was
typically better than 0.20°C (±1sd) (Fig. 7be). By comparison it was much harder to achieve a target humidity level (e.g., see
the within-experiment scatter at the two highest humidity levels in Fig. 11). Despite the challenge of controlling the humidity
of the tunnel air we were able to consistently measure the specific humidity with a precision better than 0.5 g kg^{-1} (±1sd) (Fig.
7d) in all but the most extreme conditions. At 1 bar total air pressure, 0.5 g kg^{-1} specific humidity is equivalent to a precision
410 in the vapour pressure of 80 Pa (±1sd). At 15°C the sensitivity of saturated vapour pressure to temperature is 110 Pa K^{-1} rising
to 494 Pa K^{-1} at 45°C. Hence an uncertainty in vapour pressure of 80 Pa is equivalent to an uncertainty in the theoretical wet
bulb temperature of between 0.2 to 0.7°C (i.e., 80/494 to 80/110). With that we conclude that the overall uncertainty in the
calculated wet bulb temperature is more determined by the precision of our humidity measurement than the air temperature
measurement. This result is also clearly evident by close inspection of the error bars in Fig. 10.

415

The theory used to define the wet bulb temperature here (Eqns 1 and 2) is based on concepts from classical *equilibrium*
thermodynamics and the assumption of an adiabatic enclosure (Monteith and Unsworth, 2008). However, the wind tunnel
experimental system described here is not an equilibrium system but instead operates at a steady state dis-equilibrium. The
classical adiabatic saturation psychrometer also operates in a steady state dis-equilibrium and cools air by adding water
420 (Greenspan and Wexler, 1968). Here we have essentially reversed that operation by holding the properties (temperature,
specific humidity) of the tunnel air constant and thereby cooling the shallow bath of liquid water down to a steady state
temperature that closely approximates the theoretical 'equilibrium' wet bulb temperature. More detailed theory is readily
available to analyse our steady state dis-equilibrium system (Greenspan and Wexler, 1968; Wylie, 1979; Monteith and
Unsworth, 2008) but that is not necessary here since our aim was not to have a perfect wet bulb thermometer. Instead we note
425 that the upper film-covered surface is not strictly adiabatic because it allows longwave radiative exchange across the two film

layers. That radiative exchange does not by itself invalidate the adiabatic assumption because heat has to be absorbed by the air in the tunnel to violate the constraint. However, we do anticipate a very small absorption in the 300 mm high tunnel. A further consequence of the configuration is that (sensible) heat will be conducted between the air in the tunnel and in the laboratory across the two film layers. Those two modes of heat exchanges would violate the adiabatic assumption implicit in

430 the definition of the thermodynamic wet bulb temperature and both modes of heat exchange will ultimately depend on the difference in air temperature between the tunnel and the laboratory.

The ultimate aim of the experiment is to impose a longwave forcing that is independent of the conditions in the tunnel and to measure the response of evaporation (i.e., latent heat flux) and surface temperature to that longwave forcing. The difference

435 between 'Ambient' (~ 19°C) and 'Forced' (~ 31°C) conditions is designed to impose a longwave forcing of roughly 70 W m^{-2} at the top of the film (Fig. 8b). By comparison, the measurement uncertainty for the latent heat flux is better than 2.6 W m^{-2} (±1sd) and for three-quarters of the data it is better than 1 W m^{-2} (±1sd) (Fig. 8c). Further, a formal assessment of the steady state criteria over all 90 experiments using the enthalpy storage rate had a broadly comparable result showing a range -5.0 to +3.4 W m^{-2} with an overall mean equal to zero (Fig. 9). At face value the available measurements are sufficiently precise for

440 the aim of measuring the response of evaporation to the imposed longwave forcing. The uncertainty in the incoming longwave radiation at the top of the film was reported here to be better than 4 W m^{-2} (Fig. 8d). That value was calculated directly using samples taken every 10 s over the assigned steady state period that varied from 850 to 3330 s across all experiments. However, there was a clear periodicity in the incoming longwave radiation (e.g., ~ 900 s in Fig. 5e, Fig. 6e). Given that we selected the steady state time periods to be an integer multiple of the period then the 4 W m^{-2} uncertainty estimate quoted above would be

445 an overestimate of the real uncertainty in the steady state average. However, to achieve the ultimate aims of the experiment we require knowledge of the incoming and outgoing longwave radiation *at the water surface* which requires empirical calibration of a simple radiative transfer model to account for the longwave radiative transfer through the two films as well as any influence from moist air within the tunnel. Hence the overall precision in our calculation of the incoming and outgoing longwave radiation at the water surface will largely depend on the radiative transfer model. The development and evaluation

450 of that radiative transfer model is described in a forthcoming companion article.

Author Contribution

MLR and CJS conceived the overall project and designed the experiments. AJR designed and constructed the wind tunnel. CJ carried out the experiments with assistance from MLR and AJR. MLR and CJS undertook the analysis. MLR prepared the manuscript with contributions from all co-authors.

Data Availability

The wind tunnel data is available at https://doi.org/10.5281/zenodo.7111987.

Competing Interests

The authors declare that they have no competing interests.

Acknowledgements

460 We thank Dr Chin Wong (Biology, ANU) for high level advice on the design, instrumentation and operation of the wind tunnel and Mr Peter Lanc (RSES, ANU) for developing the LabVIEW control software. The research was supported by the Australian Research Council (DP190100791).

References

Greenspan, L. and Wexler, A.: An adiabatic saturation psychrometer, Journal of Research of the National Institute of Standards, 465 72C, 33-47, 1968.

Hale, G. M. and Querry, M. R.: Optical Constants of Water in the 200-nm to 200-μm Wavelength Region, Appl. Opt., 12, 555-563, doi: 10.1364/AO.12.000555, 1973.

470 Huang, A.-N., Maeda, N., Shibata, D., Fukasawa, T., Yoshida, H., Kuo, H.-P., and Fukui, K.: Influence of a laminarizer at the inlet on the classification performance of a cyclone separator, Separation and Purification Technology, 174, 408-416, doi: 10.1016/j.seppur.2016.09.053, 2017.

Huang, J.: A Simple Accurate Formula for Calculating Saturation Vapor Pressure of Water and Ice, Journal of Applied 475 Meteorology and Climatology, 57, 1265-1272, doi: 10.1175/JAMC-D-17-0334.1, 2018.

Incropera, F. P., Dewitt, D. P., Bergman, T. L., and Lavine, A. S.: Fundamentals of Heat and Mass Transfer, 6th edition, John Wiley and Sons, Hokoben, USA, 2007.

480 Irvine, W. M. and Pollack, J. B.: Infrared optical properties of water and ice spheres, Icarus, 8, 324-360, doi: 10.1016/0019-1035(68)90083-3, 1968.

Lim, W. H., Roderick, M. L., Hobbins, M. T., Wong, S. C., Groeneveld, P. J., Sun, F., and Farquhar, G. D.: The aerodynamics of pan evaporation, Agricultural and Forest Meteorology, 152, 31-43, 2012.

485
McAlister, E. D. and McLeish, W.: Heat transfer in the top millimeter of the ocean, Journal of Geophysical Research, 74, 3408-3414, 10.1029/JC074i013p03408, 1969.

Monteith, J. L. and Unsworth, M. H.: Principles of Environmental Physics, 3rd edition, Edward Arnold, London, 2008.

490

Nunez, G. A. and Sparrow, E. M.: Models and solutions for isothermal and nonisothermal evaporation from a partially filled tube, International Journal of Heat and Mass Transfer, 31, 461-477, doi: 10.1016/0017-9310(88)90028-2, 1988.

Peixoto, J. P. and Oort, A. H.: Physics of Climate, American Institute of Physics, New York, USA, 1992.

495

Penman, H. L.: Natural evaporation from open water, bare soil and grass, Proceedings of the Royal Society of London A, 193, 120-145, 1948.

Pierrehumbert, R. T.: Principles of Planetary Climate, Cambridge University Press, Cambridge, UK, 2010.

500

Saunders, P. M.: The Temperature at the Ocean-Air Interface, Journal of the Atmospheric Sciences, 24, 269-273, doi:10.1175/1520-0469(1967)024<0269:TTATOA>2.0.CO;2, 1967.

Sparrow, E. M. and Nunez, G. A.: Experiments on isothermal and non-isothermal evaporation from partially filled, open-
505 topped vertical tubes, International Journal of Heat and Mass Transfer, 31, 1345-1355, doi: 10.1016/0017-9310(88)90244-X, 1988.

Thom, A. S., Thony, J. L., and Vauclin, M.: On the proper employment of evaporation pans and atmometers in estimating potential transpiration, Quarterly Journal of the Royal Meteorological Society, 107, 711-736, 1981.

510

Wagner, W. and Pruß, A.: The IAPWS Formulation 1995 for the Thermodynamic Properties of Ordinary Water Substance for General and Scientific Use, Journal of Physical and Chemical Reference Data, 31, 387-535, doi: 10.1063/1.1461829, 2002.

Wild, M., Folini, D., Schär, C., Loeb, N., Dutton, E., and König-Langlo, G.: The global energy balance from a surface
515 perspective, Climate Dynamics, 40, 3107-3134, doi: 10.1007/s00382-012-1569-8, 2013.

WMO: Turbulent Diffusion in the Atmosphere, World Meteorological Organisation, Geneva, SwitzerlandTechnical Note No. 24, 1977.

520 Woolf, D. K., Land, P. E., Shutler, J. D., Goddijn-Murphy, L. M., and Donlon, C. J.: On the calculation of air-sea fluxes of CO2 in the presence of temperature and salinity gradients, Journal of Geophysical Research: Oceans, 121, 1229-1248, doi: 10.1002/2015JC011427, 2016.

Wong, E. W. and Minnett, P. J.: The Response of the Ocean Thermal Skin Layer to Variations in Incident Infrared Radiation,
525 Journal of Geophysical Research: Oceans, 123, 2475-2493, 10.1002/2017JC013351, 2018.

Wylie, R. G.: Psychrometric Wet Elements as a Basis For Precise Physico-Chemical Measurements, Journal of Research of the National Bureau of Standards, 84, 161-177, 1979.

530   **Appendix A – The psychrometer constant (γ) as a function of air temperature and relative humidity**
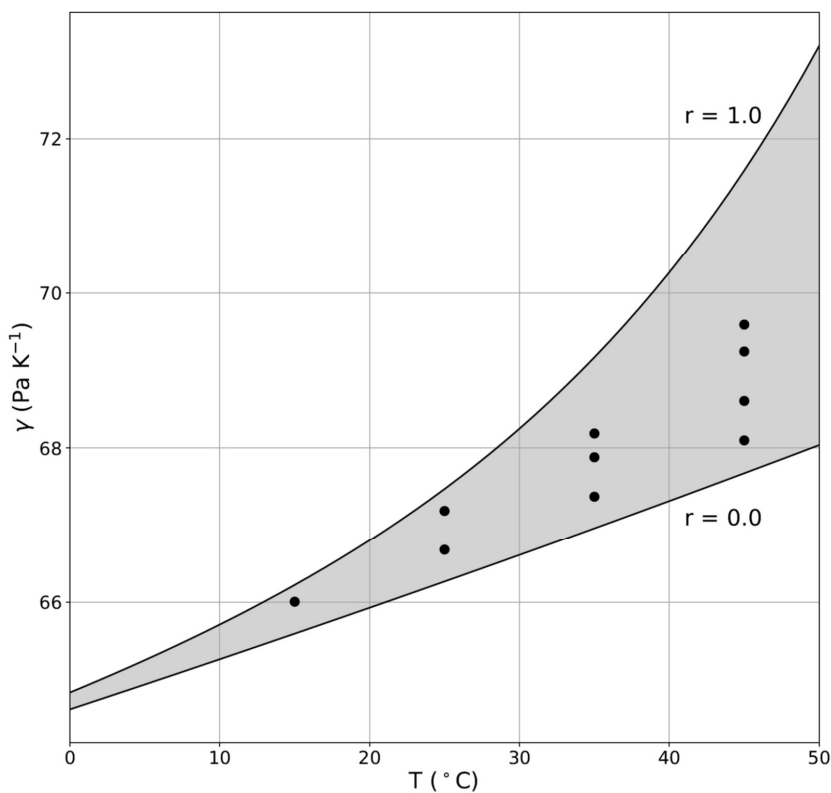
Figure A1: The psychrometer constant (γ) as a function of air temperature and relative humidity (*r*). The shaded area denotes the bounds between dry (*r* = 0.0) and saturated (*r* = 1.0) air. The dots depict the nine temperature-humidity combinations used in the experiment (Fig. 4). Total air pressure is set to 1 bar with data for specific heat and latent heat of vaporisation from the International Association for the Properties of Water and Steam (IAPWS) database (Wagner and Pruß, 2002).

535